frontiers | Frontiers in Physics

TYPE Original Research
PUBLISHED 05 May 2023
DOI 10.3389/fphy.2023.1196726

OPEN ACCESS

EDITED BY
Li Li,
Harbin Institute of Technology, China

REVIEWED BY
Baptiste Fix,
Office National d'Études et de Recherches Aérospatiales, Palaiseau, France
Jinhui Shi,
Harbin Engineering University, China

*CORRESPONDENCE
Rusnė Ivaškevičiūtė-Povilauskienė,
rusne.ivaskeviciute@ftmc.lt

RECEIVED 30 March 2023
ACCEPTED 25 April 2023
PUBLISHED 05 May 2023

CITATION
Ivaškevičiūtė-Povilauskienė R, Čižas V, Nacius E, Grigelionis I, Redeckas K, Bernatonis M, Orlov S, Valušis G and Minkevičius L (2023), Flexible terahertz optics: light beam profile engineering via C-shaped metallic metasurface. *Front. Phys.* 11:1196726. doi: 10.3389/fphy.2023.1196726

Flexible terahertz optics: light beam profile engineering via C-shaped metallic metasurface

Rusnė Ivaškevičiūtė-Povilauskienė[1]*, Vladislovas Čižas[1], Ernestas Nacius[2], Ignas Grigelionis[1], Karolis Redeckas[1], Matas Bernatonis[1], Sergej Orlov[2], Gintaras Valušis[1,3] and Linas Minkevičius[1,3]

[1]Department of Optoelectronics, Center for Physical Sciences and Technology, Vilnius, Lithuania, [2]Department of Fundamental Research, Center for Physical Sciences and Technology, Vilnius, Lithuania, [3]Department of Physics, Institute of Photonics and Nanotechnology, Vilnius University, Vilnius, Lithuania

The potential of terahertz (THz) imaging implementation in a large variety of applications requires compact, reliable, and relatively low-cost solutions in systems constituents. Here we focus on the development of passive optical elements and demonstrate flexible and reliable THz beam profile engineering for imaging aims via mechanical bending of a stainless steel-based C-shaped metasurface. The designed and laser-ablation technology fabricated metasurface provides compact THz focusing and enables THz light engineering as well as polarization control ability in THz imaging. Focusing, light profile engineering, and polarization control performances of the metasurfaces with different focal distances and C-shape designs are presented. Experimental data are well supported by simulations, using Finite Difference Time Domain (FDTD) method. THz images of different objects at ~ 94 GHz using InP Gunn diode, bow-tie sensors, and exclusively metasurfaces-based optics are exposed. Further routes in the development of low-cost multicolor and polarization-sensitive THz imaging are discussed.

KEYWORDS

terahertz, imaging, metasurfaces, compact imaging systems, mechanical bending, light profile engineering

1 Introduction

Terahertz (THz) imaging technique, due to its nondestructive origin, can serve as a powerful tool for a large variety of applications in material inspections, various security checks, or medical scanning [1, 2]. However, in the practical implementation of THz imaging systems, particular attention needs to be given to their miniaturization and optimization, enhanced functionality, reduced power consumption, and increased convenience in use [3]. It requires overcoming a number of significant obstacles related to the low power of THz emitters, the reliability of sensitive THz detectors, and effective solutions in the design and technology of passive optical components like mirrors, lenses, and beam splitters. As a rule, these elements are rather bulky, therefore, finding flat optics-based solutions can create a strong basis for the development of compact imaging systems and indicate routes for rational on-chip designs. It was demonstrated that metamaterials [4] provide unlimited rich freedom in the design of flat optical elements to manipulate features of electromagnetic waves starting from their propagation properties, polarization management, or control over the dispersion of refractive indexes of materials [5–7]. On the other hand, it was

revealed recently that THz light engineering having a strong effect on imaging properties and quality, in appropriate beam shaping schemes can outperform the conventional Gaussian illumination approach [8].

In the given work, flexible and reliable THz beam profile engineering via mechanical bending of a stainless steel-based C-shaped metasurface is presented. The designed metasurface provides compact THz focusing, light spatial profile engineering, as well as polarization control ability in THz imaging. To explore low-cost solutions in THz imaging, we have restricted ourselves to the ~ 94 GHz range relying the system on InP Gunn diode (Spacek Labs, model No: GQ-440KS), bow-tie sensors [9], and laser-ablation technology [10] fabricated metasurfaces. The study investigates the focusing, light profile engineering, and polarization control performances of metasurfaces with varying focal lengths (F = 10, 20, 30, and 40 mm) and different widths of split ring resonators SRRs (c = 30, 60, 75, and 90 μm). Experimental data are well supported by simulations using the Finite Difference Time Domain (FDTD) method. Terahertz images of different objects are exposed, and further routes in the development of low-cost multispectral and polarization-sensitive THz imaging systems are discussed.

2 Flexible optical elements and experimental setup

Any type of split ring resonator (SRR) relies on the principle of the electric field generated from the dipole or quadrupole appearing due to the charge carriers oscillating under the influence of external electromagnetic illumination [11]. In the case of the most popular type of SRRs, comprising conductive periodic structure deposited on transparent material, it can be illustrated via the dipole formation at the gap of the ring element [12]. During this study, the inverse SRR or complementary SRR (CSRR) structure, comprising periodic C-shaped openings in the conductive layer, is employed. The dipole in these structures is formed at the opening on the opposite side of the conductive gap [13]. One can note that the dipole itself can be generated due to charge carrier interaction with either separate magnetic or electric fields of the external radiation, or both, depending on how the incident radiation is applied [14]. In this study, the magnetic field vector was kept parallel to the metasurface layer, therefore, no resonance due to magnetic response can be expected, and the studied effects can be exclusively attributed to the electric resonance [15].

In any case, any SRR element can be treated as an LC circuit. Investigations dedicated to the derivation of the theoretical relations that estimate the LC parameters of any SRR structure [16, 17] allow not only to define a resonant frequency of the structure but also indicate a large variety of resonance-related phenomena, for instance, excitation of two resonance frequencies [18, 19] or frequencies shifts due to peculiarities of the meta element design [20]. The employment of the inverse (complementary) SRR structure may be of specific interest as the Babinet principle states that the diffraction pattern of the metasurface and its

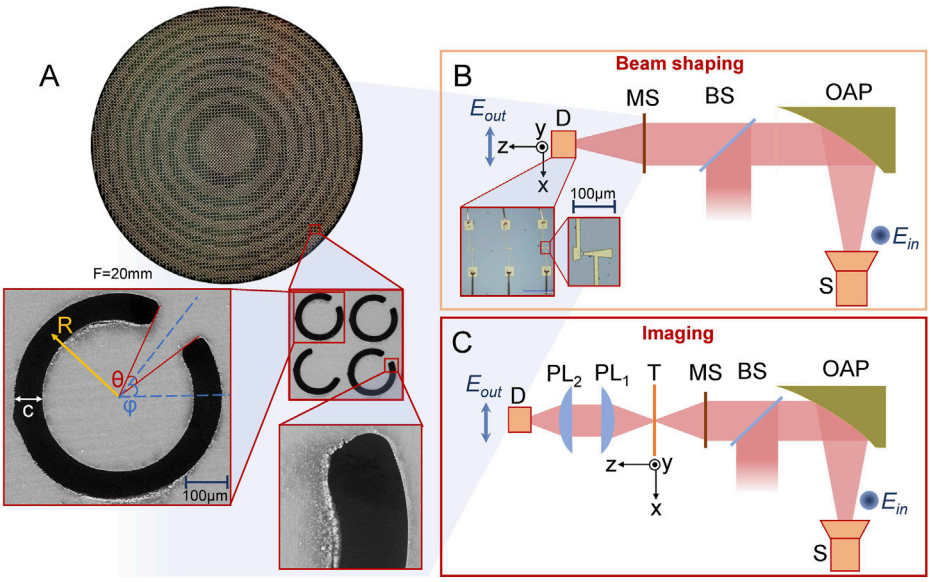

FIGURE 1
Metallic metasurface design and THz imaging setups. **(A)** Design of the metallic C-shaped complementary split-ring resonators metasurface, its geometry, and enlarged view of the metaelement depicting the parameters to be varied during this study: the letter *c* denotes the thickness of the opening, *θ* - the cutout angle, *R* is the radius, and *φ* depicts the position of the gap. **(B)** Schematic layout of the THz beam engineering setup dedicated to the evaluation of metallic metasurface design effect on the polarized light. The radiation of power of around 40 mW with an electric field polarized along the Y-axis emitted from an adjustable frequency InP Gunn diode oscillator source (Spacek Labs, model No: GQ-440KS) (S) is collimated by F = 10 cm parabolic mirror (PM) as the beam diverges. The metasurface focuses the beam onto a focal point where a polarization-sensitive InGaAs-based bow-tie-shaped detector (D) is placed. The photo of the enlarged active part of the detector is depicted in the bottom inset. A high resistivity silicon beam splitter (BS) of 525 μm thickness is placed between a parabolic mirror and metallic metasurface in order to reduce the standing wave effects between the emitter and metallic metasurface. **(C)** THz imaging setup employing the THz beam engineering. The setup contains two additional paraffin lenses (PL1 and PL2) dedicated to collimate the THz beam after it passes through the target (T) and then focusing it into the detector.

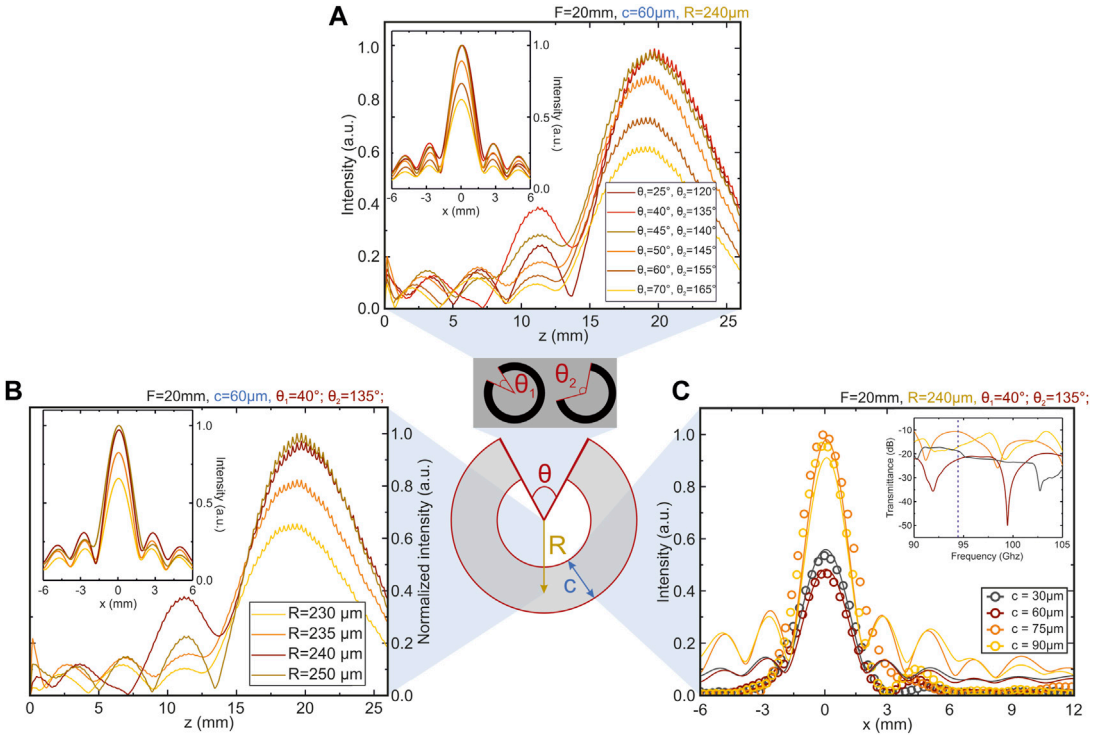

FIGURE 2
The dependence of CSRR metasurface focusing performance on different metacell geometrical parameters. **(A)** Simulation of the intensity distribution along the optical axis, obtained by varying cutout angles θ_1 and θ_2. Intensities along the *x*-axis at the focal plane are displayed in the inset. The optimal pair of angles θ_1=40° and θ_2=135° was selected for the following simulations. **(B)** Simulations of intensity distribution along the optical axis for the CSRRs metaelement radius *R* ranging from 230 μm to 250 μm. Intensities along the *x*-axis at the focal plane are displayed in the inset. The optimal radius of *R* =240 μm was selected for the following simulations. **(C)** Illustration of the experimentally measured (symbols) and simulated (solid line) intensities along *x*-axis at the focal plane for the varying opening widths of the metaelements, denoted by the letter *c* at the central image. The inset denotes the simulated transmission spectra of the CSRR structure at the focal point, the blue dashed line represents the frequency used during the experiments. In all cases, fixed parameters are displayed in the insets of the relevant panels.

complementary metasurface is the same [21, 22]. This fact establishes the background for the development of the CSRR structure as a focusing element with the same focal length at the same resonant frequency as the conventional SRR [23]. Furthermore, this allows extending the beam shaping facilities using CSRR as metaelements employing experience of studies in more classic metasurfaces [24–27].

Investigated metasurface containing CSRRs was manufactured from a 25 μm thickness stainless steel foil employing laser-ablation technology, already successfully applied for compact THz optics fabrication aims [10, 28]. The ablation process was carried out by using Pharos SP (produced by Light Conversion Ltd.) laser, delivering ultrashort pulses of duration tunable from 158 fs to 10 ps at λ = 1030 nm wavelength with a maximum average power of 6 W at 200 kHz repetition rate. The beam positioning system intelliSCAN (Scanlab), paired with the f-theta lens of effective focal length f = 100 mm, was used to scan and focus the beam onto the surface of the foil. To keep the heat-affected zone as small as possible during the ablation, low pulse energy with a high scanning speed combination was used. Scanning was done with pulse density of 200 mm^{-1} under peak fluence of F = 9.4 J/cm^2 and repeating at least 250 times for a single feature to fully cut through the substrate. Such selection of parameters helped to maintain the flat surface of the foil unaffected by excess heat and to avoid oxidation. After the microfabrication, the sample was immersed in an ultrasonic bath in order clean off the built-up debris from its surface.

The complementary metasurface's openings were systematically placed in a recurring design based on the 5 zones and 4 subzones Fresnel equation [29] to act as a zone plate (top panel of Figure 1A) enabling a possibility to focus and manipulate the THz light beam. The CSRRs gap's position and cutout angle (described by φ and θ, respectively, in the bottom left part of Figure 1A) were adjusted relying on their location on the metasurface, aiming to achieve the required phase-shift for each CSRR. Each subzone of the zone plate was filled with identical CSRR metaelements, ensuring π/2 phase shift between the neighbouring zones. Furthermore, the radius of the openings (R) and their width (c) were varied for further optimization of the focusing element. It is deserved noting that the detected signal is due to radiation re-emission from the metasurface only. In this case, the ratio of exciting and re-emission powers is metasurface rotation angle-dependent and amounts to 6%–10%.

Figure 1B shows a schematic layout of the THz beam engineering setup, dedicated to investigating the designed metallic metasurfaces. The setup is based on an adjustable InP Gunn diode oscillator delivering tunable frequency radiation in

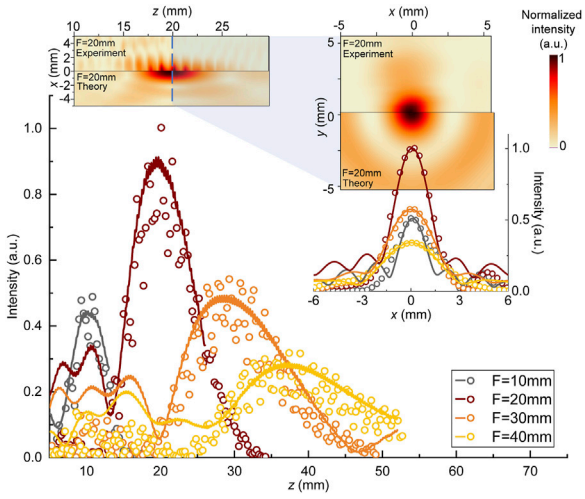

FIGURE 3
Focusing performances of the complementary C-shaped split ring resonators-based metasurface with different focal lengths (F =10,20,30, and 40 mm) at ~ 94 GHz. The main graph–experimental results (symbols) and simulation results (solid lines) of the beam profile distribution along the optical axis for metasurfaces of the different focal lengths. Top left inset–the performance of the metasurface lens with the focal length of 20 mm: top half represents experimentally obtained and bottom half depicts simulated intensity distribution of THz beam along the optical axis. Note the standing wave effect occurring in the experimental part. The blue line indicates the focus position of the analyzed CSRR structure. The upper part of the top right inset–THz beam intensity distribution in the focal plane corresponding to the blue dashed line of the top left inset. The top half depicts experimental results and bottom half–theoretical simulations. The bottom part corresponds to the intensity beam profile along the x-axis at the focal point of the metasurfaces with different focal lengths, where the experimental results are marked as symbols and theoretical simulations are depicted as solid lines.

the interval of 93.8 GHz–94.1 GHz, passive optical elements, and bow-tie diode as the THz sensor, a photo of the detector is given in the left-bottom inset of Figure 1B. The latter device is based on the molecular-beam-epitaxy-grown InGaAs structure (sample I198:058 525 nm-thick $In_{0.46}Ga_{0.54}As$) and fabricated using procedures described in detail in Ref. [30]. The inherent feature of the device is the broadband operation with an almost flat response up to 0.8 THz [9]. As the sensor resembles a bow-tie antenna, it exhibits good coupling and nanoseconds duration response in free space at 94 GHz [31]. Figure 1C shows the schematic layout of the THz imaging setup, which contains two additional paraffin lenses, dedicated to collimating the THz beam after it passes through the target and then focusing it into the detector.

3 Experimental results and discussion

The primary objective was to determine the effect on the focusing abilities of the CSRR metasurface by variation of different CSRR metaelement parameters, depicted at the centre of Figure 2. The starting parameters, adapted for the desired frequency were taken from similar studies of another group [26]. Aiming to produce the most efficient focusing metasurfaces operating around ~94 GHz, numerical simulations, varying the cutout angle, were conducted with focal length F = 20 mm, R = 240 μm radius, and c = 60 μm opening width (Figure 2A). The cutout angles of two different metaelements were varied keeping a constant relative phase shift of $\pi/2$. Additionally, employing the determined optimal cutout angle, the effect of different CSRR's metaelement radius (R) was simulated (Figure 2B). Finally, the variation of CSRRs width (c) as 30, 60, 75 and 90 μm was performed for the F = 20 mm, R = 240 μm and cutout angles of $\theta_1 = 40^{\circ}$ and $\theta_2 = 135^{\circ}$. The metasurfaces with identical parameters were also investigated experimentally. The simulation-matching results, depicted in Figure 2C, reveal that the best focusing was achieved with the opening width of c = 75 μm. The metasurfaces, containing metaelements with all three optimized parameters were used for the following studies of different focal length structures and the metasurface bending effect on the focusing performance.

Four metasurfaces with different focal lengths of F = 10, 20, 30, and 40 mm have been fabricated, and their focusing performance was investigated both experimentally and theoretically. Experimentally obtained THz beam intensity distribution along the optical axis is depicted in the main graph of Figure 3 and is represented by symbols. The operation of metasurfaces as well as properties of propagating THz light was theoretically modeled using the FDTD method presented by straight lines. As one can see, the intensity of the beam, focused with F = 20 mm focal length metasurface, expresses sharply increased intensity in comparison to other designs with F = 10 mm, F = 30 mm, and F = 40 mm. Several aspects need to be taken into account analyzing these results. It is worth noting that the incident radiation excites dipole and quadrupole moments in the CSRR structure which signatures, as it will be shown later, become pronounced in angular dependencies of the re-emitted pattern [32]. The performance of a single metaelement can be explained using the concept of the numerical aperture (NA), which is NA = $\sin(\theta)$, where $\theta = \arctan(D/2f)$ is the largest meridional angle of the ray reaching the focal point (f - focal length, D - entrance pupil). The dipole wave radiation is not distributed isotropically in space. Like in a dipole antenna, the radiation directrix of the metacell obeys the squared cosine law in regard to the meridional angle (the direction at which rays arrive at the collective focus) [32]. Thus, the CSRR radiates around the directions lying perpendicular to the excited dipole moment because of the non-spherical electric and magnetic waves re-emitted from the structure. In the case of the zone plates with short focal distances (i.e., large NA) it means that the rays arriving at the focus have amplitudes modulated by the directrix function of the CSRR. The second effect which further decreases the intensity of the radiation in nonparaxial focal points is caused by the paraxial design of the zone plate. A variety of aberrations are introduced through, for example, the aplanatic factor - the rays arriving at the focal spot at larger spatial angles impinge the focus and are bent too much, therefore, their amplitudes are further modulated by the meridional angle.

As the focal distances increase, the NA decreases, thus, the aforementioned effects become less pronounced and the conventional behaviour of the Gaussian beam is observed. What is more, with an increase of the focal distance, the size of the Gaussian beam and its Rayleigh distance $z_r = k\omega_0^2/2$ also increases, therefore, the volume occupied by the beam is

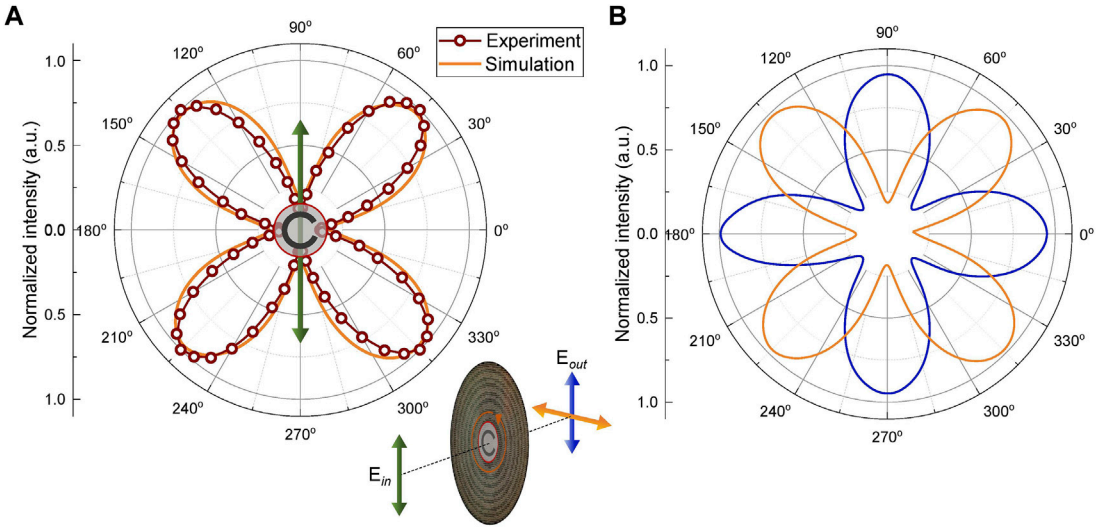

FIGURE 4
(A) Angular dependency of the recorded electric field component of the illumination on the rotation angle of the metasurface structure. Note that the polarization of the incident THz light is perpendicular to the recorded one (cf. orange arrow at the bottom right inset) as the rotation of the structure consequently changes the orientation of the dipole moment leading to the generation of the electric field component perpendicular to the direction of the incident electromagnetic field. The metaelement in the center of the graph depicts the 0° position of the central Fresnel subzone of the structure. The solid line with symbols represents experimental data while the thick solid line depicts simulation results. In the inset, the green arrow marked as E_{in} corresponds to the polarization of the incident THz light, the orange arrow marks the recorded THz light, which is perpendicularly polarized to the incident light, and the blue arrow marks the recorded THz light, which is polarized in parallel to the incident light. **(B)** The simulated angular dependency of the electric field of two different polarizations on the angle corresponding to the position of the conductive gap of the metacell in the structure. The color of the solid line depicts the simulated polarization according to the inset of the panel (A). The differences in angular electric field dependencies allow employing polarization-resolved imaging.

$V = k\pi\omega_0^4/2$, and the maximal intensity decreases in the expected manner ($k = 2\pi/\lambda$ - wave number, ω_0 is the beam waist). This effect is further intensified due to fixed-size 2-inch steel wafers used for the production, resulting that for the case of longer focal distance, the dimensions of the full 5 zones, 4 subzones Fresnel lens structure exceeds the 2-inch wafer size, therefore, it further decreases the intensity and the Rayleigh length.

The top left inset in Figure 3 shows the performance of the metasurface at the best operational focal point of $F = 20$ mm. The top half presents experimentally obtained and the bottom half depicts the simulated intensity distribution of THz beam along the optical axis. In contrast to the theoretical simulations, the experimental beam intensity distribution shows the presence of Fabry-Perot oscillations due to the formation of the standing waves. This discrepancy is due to different boundary conditions: in simulations, it is assumed that the waves, reflected from the metasurface, are absorbed, whereas in an experiment the waves experience the reflection from the beam splitter plate (cf. BS at Figure 1B) The top right inset depicts the THz beam profile in the focal plane (xy) of metasurfaces with different focal lengths. The best performance of $F = 20$ mm metasurface is compared with relevant simulations. The top half presents experimentally obtained results whereas the bottom half depicts numerical simulations. As it is seen, the theory describes the measurement data well.

As was aforesaid, the CSRR operation relies on dipole- and quadrupole-based re-emission of the incident THz radiation which is dependent on the angle between the E-field of the incident illumination and the CSRR gap, allowing thus the effect of polarization-sensitive focusing. To evidence it, we rotate CSRRs metasurface to measure the angular dependencies of the re-emitted THz radiation intensity. The angular dependency of the re-emitted electric field component, which is perpendicular-polarized to the incident THz radiation, is shown in Figure 4A. The intensity peaks are achieved when the angle between the CSRRs gap and incident electric field component is 45°, 135°, 225° and 315°. These observations, supported by FDTD simulations are consistent, taking into account the geometry of the above-described dipole formation in the CSRR metaelements. Consequently, such distribution enables a significant increase in signal-to-noise ratio for THz imaging systems operating in the transmission geometry. The bottom right inset depicts the polarization rotation features of the metasurface. The green arrow corresponds to the polarization of the incident THz radiation and the orange arrow indicates the polarization of the detected THz radiation. Considering angular dependency of the polarization, parallel to the incident THz radiation, depicted as a blue arrow in the inset of Figure 4A, one may note the 45° peak position shift, depicted as simulation results in Figure 4B. Typically, a single metacell would manifest a $\pi/2$ intensity symmetry for the perpendicular polarization (orange arrow) and π intensity symmetry for the parallel one (blue arrow). However, as the metaelements in the subzones 3 and 4 of each Fresnel zone are 90° rotated copies of the subzones 1 and 2 respectively, the final angular dependency for both polarization expresses $\pi/2$ symmetry with 45° intensity shift between the polarizations (Figure 4B). Such

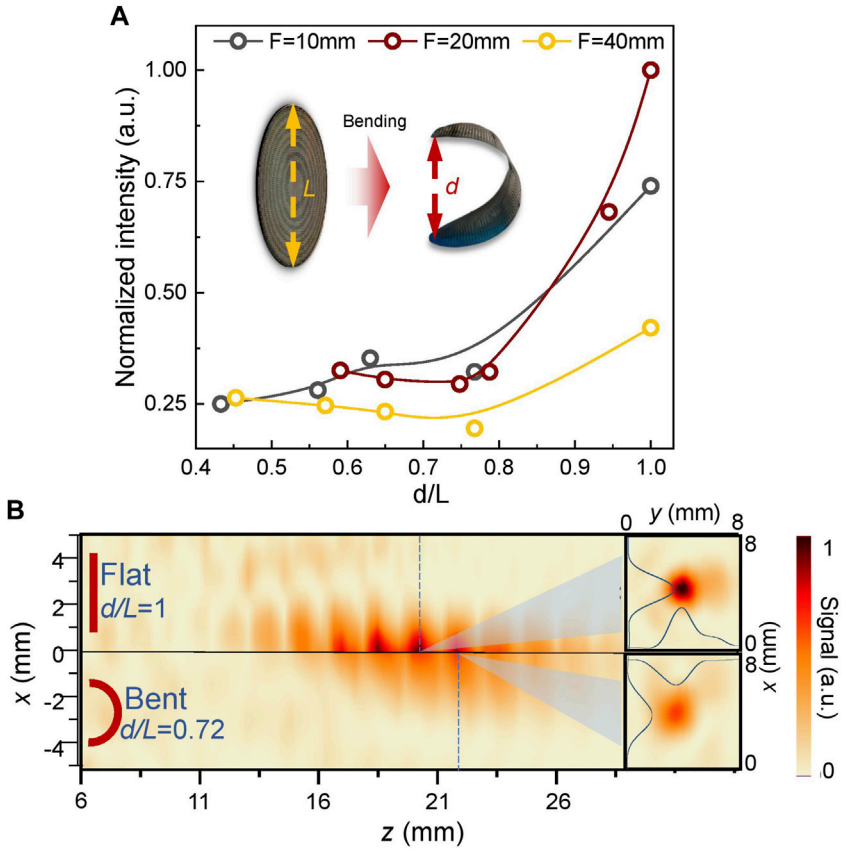

FIGURE 5
(A) Measured intensity dependence upon bending metasurfaces of different focal lengths. The inset depicts a visualization of the bent metasurface. Letter *L* denotes the diameter of the unbent metasurface and *d* is the distance between two opposite ends of the deformed plate. The bending level is represented as a ratio of *d*/*L*. **(B)** Intensity distribution of the THz beam along the optical axis (*xz*): the top half represents results when the metasurface was flat and the bottom half when the metasurface was bent. The dashed blue lines indicate the focus position. Note the change of the focal distance and intensity occurring due to bending, giving additional adjustment ability. Insets on the right side represent beam intensity distribution in the focal plane (*xy*) for the cases when the metasurface is flat and bent, respectively.

peculiarities of the structure allow for further enhanced imaging possibilities employing metasurfaces, as described below.

Another explored peculiarity of the CSRR structure, unavailable for the standard SRR, is structure bending ability. The flexibility of the metallic metasurface CSRRs not only allows them to maintain their functionality upon bending as an optical element but also provides tunability options for focusing and light manipulation under variations of mechanical deformation. To illustrate this, metasurfaces were investigated experimentally in a flat geometry and under variation of mechanical bending. The bending is represented by the *d*/*L* ratio, where *d* is the distance between the opposite ends of the deformed plate, and *L* is the diameter of the flat metasurface.

Signal dependency on the mechanical metasurface bending (*d*/*L*) is shown in Figure 5A. Three different metasurfaces designed for the focal lengths of (F = 10, 20, and 40 mm) were investigated. As was discussed in Figure 3, without mechanical deformation, the metasurface with F = 20 mm provides the highest signal. With the increase of mechanical bending, the recorded signal decreases in all the cases, however, the focusing ability of the structure remains. At the maximum bend, $d/L \approx 0.45$, all investigated structures reach similar signal values, amounting to $\approx 25\%$ of the maximum signal with respect to the best flat metasurface with focal length F = 20 mm. Although the focal point changes its position due to the bending, the shape of the beam remains the same. It is evident from the plot depicted in Figure 5B, representing experimentally obtained flat and bent intensity distributions along the optical axis (*xz* plane), and right insets displaying experimental data of the intensity distribution in the focal (*xy*) plane. Therefore, the focusing abilities and focus tunability of CSRR-based optics elements via mechanical bending extend the area of different applications in the further development of compact THz imaging systems containing flexible optics.

4 THz imaging using C-shaped metasurface

THz imaging performance of the metasurface designed for F = 20 mm is presented in Figure 6. Images were recorded using the setup, depicted in Figure 1C, where two non-transparent samples were raster-scanned during the THz illumination by the investigated metasurface. The first sample, comprising metallic target featuring cutout slits with varying widths (3 mm, 2 mm, and 1.5 mm) organized

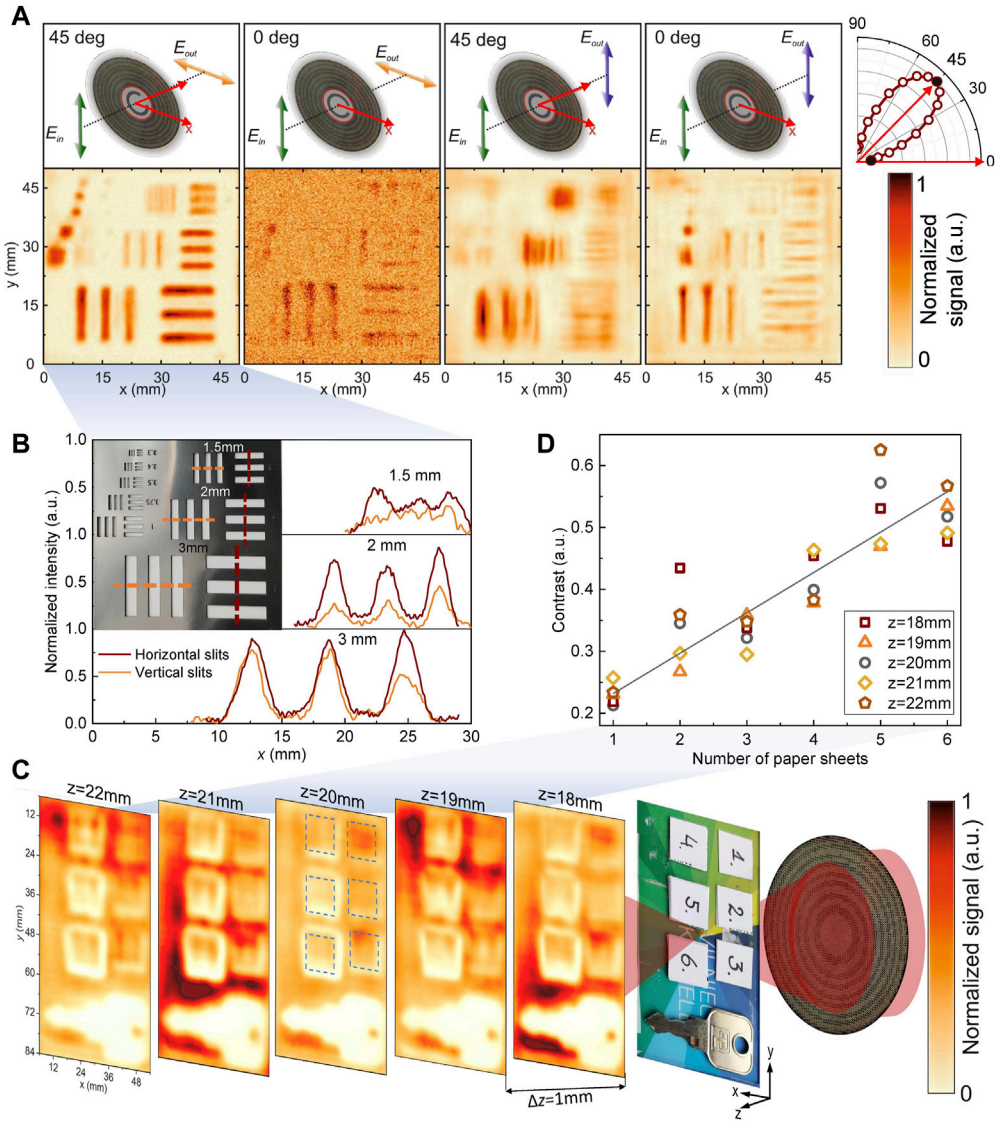

FIGURE 6
Demonstration of THz imaging using the focusing metasurface with the focal length of F =20 mm. **(A)** Imaging of a metallic target with different period slits is achieved by recording different polarizations with the metasurface rotated either 0° or 45°. The color scale indicates the signal, normalized to its maximum value. Setups are depicted above each relevant imaging picture. The top right corner inset depicts the perpendicular-polarized electric field component dependence on the angle of the metasurface. The intensities, corresponding to the angle of the metasurface in this imaging experiment, are indicated by black dots. **(B)** Cross-sections of different period slits orientated vertically and horizontally at the positions denoted by the dashed lines for the case of the most left image of panel A. Inset shows a photograph of the imaged target. **(C)** Imaging of a special sample made of a plastic card containing a metal key and a different number (1–6) of paper sheets. During the imaging, the metasurface was used to focus the THz radiation onto the sample. Each image is obtained by moving the sample along the optical axis away from the focal plane of the metasurface with the step of 1 mm. The color scale indicates the signal normalized to its maximum value. **(D)** Contrast dependence on the number of paper sheets at different sample positions along the optical axis.

into groups according to their period, is depicted in the inset of Figure 6B. Each group of slits contains a 90° rotated duplicate so that the slits are oriented vertically and horizontally. Furthermore, as demonstrated later, the imaging of the target results in an object geometry that is responsive to variations in THz polarization on the other hand, it gives the possibility to determine the spatial resolution of the resulting images using the CSRR structure.

Figure 6A depicts the imaging results of the first sample, achieved by recording different polarizations with the metasurface rotated either 0° or 45°. The imaging setup is depicted above each relevant imaging picture, and the metasurface rotation angle is indicated on each top left angle of the setup. For the aim of convenience and clarity, the theoretical angular dependence of the perpendicularly polarized component is given in the right inset of panel (A). Perpendicular polarization-resolved imaging features can be seen from two left images of Figure 6A. In the left image, the metasurface is rotated by 45°, resulting in the peak of perpendicular polarization intensity (cf. Figure 4 and the right inset). One may note that horizontal lines are much more clearly

resolved in comparison to the vertical lines of the same period. This is because the perpendicular-polarized radiation is dominant in such setup geometry. The exception are the largest (3 mm) slits where almost no difference is visible between the different orientations as the slits are wide enough to resolve the parallel polarization. By rotating the metasurface by an additional 45° into 0° degree position, we get the minimal generation of the perpendicular-polarized radiation, therefore, nearly no imaging is possible as it is depicted on the second left imaging of Figure 6A. These results are further manifested by Figure 6B, where the intensity profiles of the most left image are taken for the different width slits at the lines depicted in the inset. The possibility to distinguish the slit at each profile for the case of perpendicular-polarized setup, results in 0.5λ spatial resolution.

The situation becomes different in the case of parallel-polarized radiation (two right images of Figure 6A). For the case when metasurface is rotated by 45° degrees (the second right image), some blurred picture is visible, but no clear picture is resolved, as the intensity of the parallel-polarized component is very low, and the focal point of this polarization is more diffused compared to the perpendicular-polarized one. Still, by rotating the metasurface back to 0° (the case when the conductive gap is arranged along the *x*-axis) where the parallel-polarized radiation experiences a peak, we may achieve a parallel-polarized resolved image, manifested in highlighted vertical lines (most right image of Figure 6A). The target was additionally imaged by varying its distance from the metasurface focal plane by 1 mm steps. The spatial resolution was determined at each position, reaching 0.5λ in all the cases, showing that the resolution remains the same regardless of the sample position within at least 5 mm range. This implies that such a metasurface enables high-quality images even if the imaged sample is not located precisely at the focal plane.

The second sample depicted in Figure 6C, was a plastic card with included a metal key and six areas containing a different number of paper sheets, varying from 1 to 6. In order to determine the effect of misalignment on imaging quality, the scanning process was repeated by moving the sample away from the metasurface focal plane with 1 mm step as in the previously described process of determination of spatial resolution. The contrast values are defined as $C = (I_B - I_S)/(I_B + I_S)$, where I_S is the average intensity at the largest signal area and I_B labels average intensity at the minimal signal area were calculated for each sample position in the optical axis and for different numbers of paper sheets. Contrast dependence on the number of paper sheets and the position of the sample presented in Figure 6D. The results show that the contrast remains very similar regardless of the out-of-focus distance for each number of paper sheets. This implies that good image quality can be obtained even if the metasurface-based imaging is significantly detuned from the focal point. This illustrates the operational flexibility of metasurfaces opening hence a possibility to deploy them in industrial THz imaging systems, where precise optical alignment and tunability of optical components is not possible or hard to achieve.

5 Conclusion

The proposed approach revealed promising features of mechanically deformable metasurfaces for THz light manipulation opening thus a new route for the implementation of flexibly reconfigurable metasurfaces into the further development of compact THz imaging systems. Metasurfaces based on C-shaped complementary split-ring resonators manufactured from a 25 µm thickness stainless steel foil employing laser-ablation technology were applied for compact THz optics aims. Mechanical bending as a tool to manipulate the intensity and focusing properties of THz illumination is investigated. Polarization control via complementary C-shaped metasurfaces was presented at 94 GHz, and polarization-resolved THz imaging was demonstrated with the spatial resolution of half of the wavelength. It is shown that mechanically deformable metasurfaces can provide a dimension of operational flexibility opening hence an optimistic option to implement them in industrial THz imaging systems, where precise optical alignment is hard to achieve.

The approach can successfully be extended for multispectral THz imaging [33] aims thus enabling the wider scale of more precise identification of packaged objects contents or for modulation and manipulation of THz wavefront via a proper selection of a relevant metasurface with a liquid crystal elastomer [34].

Data availability statement

The original contribution presented in the study are included in the article, further inquiries can be directed to the corresponding author.

Author contributions

Conceptualization of the research, GV, VČ, and LM; methodology, IG and VČ; software, VČ, IG, and SO; sample ablation, EN; sample preparation, KR and MB; investigation using THz imaging set up, RI-P, KR, MB, and LM; polarization theoretical and experimental investigation, VČ and IG; data acquisition, IG, LM, and RI-P; experimental data analysis, GV, IG, VČ, and LM; writing—original draft preparation, IG, RI-P, and VČ; writing—review and editing, RI-P, VČ, IG, SO, GV, and LM; visualization, VČ, RI-P, and KR; supervision and coordination, GV and LM; project administration, LM; All authors have read and agreed to the published version of the manuscript.

Funding

This research has received funding from the Research Council of Lithuania (LMTLT), agreement No. (S-MIP-22-76).

Acknowledgments

The authors are grateful to Prof. Vincas Tamošiūnas for illuminating discussions and Dr. Domas Jokubauskis for his kind technical assistance.

Conflict of interest

The authors declare that the research was conducted in the absence of any commercial or financial relationships that could be construed as a potential conflict of interest.

Publisher's note

References

1. Mittleman DM. Twenty years of terahertz imaging [Invited]. *Opt Express* (2018) 26: 9417–31. doi:10.1364/oe.26.009417

2. Castro-Camus E, Koch M, Mittleman DM. Recent advances in terahertz imaging: 1999 to 2021. *Appl Phys B: Lasers Opt* (2022) 128:12. doi:10.1007/s00340-021-07732-4

3. Valušis G, Lisauskas A, Yuan H, Knap W, Roskos HG. Roadmap of terahertz imaging 2021. *Sensors* (2021) 21:4092. doi:10.3390/s21124092

4. Pendry J, Holden A, Robbins D, Stewart W. Magnetism from conductors and enhanced nonlinear phenomena. *IEEE Trans Microwave Theor Tech* (1999) 47: 2075–84. doi:10.1109/22.798002

5. Chen WT, Zhu AY, Capasso F. Flat optics with dispersion-engineered metasurfaces. *Nat Rev Mater* (2020) 5:604–20. doi:10.1038/s41578-020-0203-3

6. Dorrah AH, Rubin NA, Zaidi A, Tamagnone M, Capasso F. Metasurface optics for on-demand polarization transformations along the optical path. *Nat Photon* (2021) 15: 287–96. doi:10.1038/s41566-020-00750-2

7. Hu J, Bandyopadhyay S, Liu Y, Shao L. A review on metasurface: From principle to smart metadevices. *Front Phys* (2021) 8. doi:10.3389/fphy.2020.586087

8. Ivaškevičiūtė-Povilauskienė R, Kizevičius P, Nacius E, Jokubauskis D, Ikamas K, Lisauskas A, et al. Terahertz structured light: Nonparaxial airy imaging using silicon diffractive optics. *Light: Sci Appl* (2022) 11:326. doi:10.1038/s41377-022-01007-z

9. Seliuta D, Kašalynas I, Tamošiūnas V, Balakauskas S, Martūnas Z, Ašmontas S, et al. Silicon lens-coupled bow-tie InGaAs-based broadband terahertz sensor operating at room temperature. *Electro Lett* (2006) 42:825. doi:10.1049/el:20061224

10. Minkevičius L, Indrišiūnas S, Šniaukas R, Voisiat B, Janonis V, Tamošiūnas V, et al. Terahertz multilevel phase Fresnel lenses fabricated by laser patterning of silicon. *Opt Lett* (2017) 42:1875–8. doi:10.1364/OL.42.001875

11. Hein SM, Giessen H. Tailoring magnetic dipole emission with plasmonic split-ring resonators. *Phys Rev Lett* (2013) 111:026803. doi:10.1103/PhysRevLett.111.026803

12. Hesmer F, Tatartschuk E, Zhuromskyy O, Radkovskaya AA, Shamonin M, Hao T, et al. Coupling mechanisms for split ring resonators: Theory and experiment. *physica status solidi (b)* (2007) 244:1170–5. doi:10.1002/pssb.200674501

13. Song Z, Zhao Z, Zhao H, Peng W, He X, Shi W. Teeter-totter effect of terahertz dual modes in c-shaped complementary split-ring resonators. *J Appl Phys* (2015) 118: 043108. doi:10.1063/1.4927845

14. Gay-Balmaz P, Martin OJF. Electromagnetic resonances in individual and coupled split-ring resonators. *J Appl Phys* (2002) 92:2929–36. doi:10.1063/1.1497452

15. Schurig D, Mock JJ, Smith DR. Electric-field-coupled resonators for negative permittivity metamaterials. *Appl Phys Lett* (2006) 88:041109. doi:10.1063/1.2166681

16. Sydoruk O, Tatartschuk E, Shamonina E, Solymar L. Analytical formulation for the resonant frequency of split rings. *J Appl Phys* (2009) 105:014903. doi:10.1063/1.3056052

17. Wu G, Zhang Y, Huang C. Improved circuit model for plasmonic resonance of single split-ring resonators. *AIP Adv* (2022) 12:115304. doi:10.1063/5.0125608

18. Zahertar S, Yalcinkaya AD, Torun H. Rectangular split-ring resonators with single-split and two-splits under different excitations at microwave frequencies. *AIP Adv* (2015) 5:117220. doi:10.1063/1.4935910

19. Zheng X, Zhao Z, Song Z, Peng W, Zhao W, He X, et al. The influence of element deformation on terahertz mode interaction in split-ring resonator-based meta-atoms. *Plasmonics* (2017) 12:1391–8. doi:10.1007/s11468-016-0398-8

20. Hokmabadi M, Philip E, Kung RPE, Kim S. Plasmon-induced transparency by hybridizing concentric-twisted double split ring resonators. *Sci Rep* (2015) 5:15735. doi:10.1038/srep15735

21. Falcone F, Lopetegi T, Laso MAG, Baena JD, Bonache J, Beruete M, et al. Babinet principle applied to the design of metasurfaces and metamaterials. *Phys Rev Lett* (2004) 93:197401. doi:10.1103/PhysRevLett.93.197401

22. Jackson JD. *Classical electrodynamics*. Hoboken: John Wiley & Sons Inc. (1998).

23. Chen H, O'Hara J, Taylor A, Averitt R, Highstrete C, Lee M, et al. Complementary planar terahertz metamaterials. *Opt Express* (2007) 15:1084–95. doi:10.1364/oe.15.001084

24. Zhang X, Tian Z, Yue W, Gu J, Zhang S, Han J, et al. Broadband terahertz wave deflection based on c-shape complex metamaterials with phase discontinuities. *Adv Mater* (2013) 25:4567–72. doi:10.1002/adma.201204850

25. Liu L, Zhang X, Kenney M, Su X, Xu N, Ouyang C, et al. Broadband metasurfaces with simultaneous control of phase and amplitude. *Adv Mater* (2014) 26:5031–6. doi:10.1002/adma.201401484

26. He J, Ye J, Wang X, Kan Q, Zhang Y. A broadband terahertz ultrathin multi-focus lens. *Sci Rep* (2016) 6:28800. doi:10.1038/srep28800

27. Hashemi M, Moazami A, Naserpour M, Zapata-Rodríguez CJ. A broadband multifocal metalens in the terahertz frequency range. *Opt Commun* (2016) 370:306–10. doi:10.1016/j.optcom.2016.03.031

28. Minkevičius L, Jokubauskis D, Kašalynas I, Orlov S, Urbas A, Valušis G. Bessel terahertz imaging with enhanced contrast realized by silicon multi-phase diffractive optics. *Opt Express* (2019) 27:36358. doi:10.1364/oe.27.036358

29. Hristov HD, Rodriguez JM, Grote W. The grooved-dielectric Fresnel zone plate: An effective terahertz lens and antenna. *Microwave Opt Technol Lett* (2012) 54:1343–48. doi:10.1002/mop.26812

30. Minkevičius L, Tamošiūnas V, Kojelis M, Žąsinas E, Bukauskas V, Šetkus A, et al. Influence of field effects on the performance of InGaAs-based terahertz radiation detectors. *J Infrared, Millimeter, Terahertz Waves* (2017) 38:689–707. doi:10.1007/s10762-017-0382-1

31. Kašalynas I, Seliuta D, Simniškis R, Tamošiunas V, Köhler K, Valušis G. Terahertz imaging with bow-tie InGaAs-based diode with broken symmetry. *Electro Lett* (2009) 45:833–5. doi:10.1049/el.2009.0336

32. Stratton JA. *Electromagnetic theory*, 33. Hoboken: John Wiley & Sons (2007).

33. Kasalynas I, Venckevicius R, Valusis G. Continuous wave spectroscopic terahertz imaging with ingaas bow-tie diodes at room temperature. *IEEE Sensors J* (2013) 13:50–4. doi:10.1109/JSEN.2012.2223459

34. Zhuang X, Zhang W, Wang K, Gu Y, An Y, Zhang X, et al. Active terahertz beam steering based on mechanical deformation of liquid crystal elastomer metasurface. *Light: Sci Appl* (2023) 12:14. doi:10.1038/s41377-022-01046-6